Chapter 16
Urban Pollution

Janet E. Nichol, Muhammad Bilal, Majid Nazeer, and Man Sing Wong

Abstract   This chapter depicts the state of the art in remote sensing for urban pollution monitoring, including urban heat islands, urban air quality, and water quality around urban coastlines. Recent developments in spatial and temporal resolutions of modern sensors, and in retrieval methodologies and gap-filling routines, have increased the applicability of remote sensing for urban areas. However, capturing the spatial heterogeneity of urban areas is still challenging, given the spatial resolution limitations of aerosol retrieval algorithms for air-quality monitoring, and of modern thermal sensors for urban heat island analysis. For urban coastal applications, water-quality parameters can now be retrieved with adequate spatial and temporal detail even for localized phenomena such as algal blooms, pollution plumes, and point pollution sources. The chapter reviews the main sensors used, and developments in retrieval algorithms. For urban air quality the MODIS Dark Target (DT), Deep Blue (DB), and the merged DT/DB algorithms are evaluated. For urban heat island and urban climatic analysis using coarse- and medium- resolution thermal sensors, MODIS, Landsat, and ASTER are evaluated. For water-quality monitoring, medium spatial resolution sensors including Landsat, HJ1A/B, and Sentinel 2, are evaluated as potential replacements for expensive routine ship-borne monitoring.

J. E. Nichol (✉) · M. S. Wong
Department of Land Surveying and Geo-Informatics, The Hong Kong Polytechnic University, Hong Kong, China
e-mail: janet.nichol@connect.polyu.hk

J. E. Nichol
Department of Geography, University of Sussex, Brighton, UK

M. Bilal
School of Marine Sciences, Nanjing University of Information Science and Technology, Nanjing, China

M. Nazeer
Key Laboratory of Digital Land and Resources, East China University of Technology, Nanchang, China

Earth and Atmospheric Remote Sensing Lab (EARL), Islamabad, Pakistan

16.1   Monitoring Air Quality in Urban Areas

The gathering of air-quality data for urban areas and their source regions is a major challenge because the large areas involved cannot be represented by ground stations. Although satellite sensing systems and methodologies have recently been developed with an adequate spectral and temporal resolution for monitoring aerosols, it is difficult to obtain fine spatial resolution because the atmospheric signal being sensed is only a small proportion of the total image reflectance; thus large areas corresponding to large pixels, giving a higher measurable signal, are required.

The most accessible remotely sensed parameter of air quality is aerosol optical depth (AOD). This is a unit-less measure of the total amount of aerosol in the atmospheric column and is based on the opacity of the atmosphere in a particular waveband. There is no general algorithm which can retrieve aerosol properties over every kind of surface. Instead, different algorithms have been developed for (i) water, (ii) dark vegetation, (iii) bright surfaces, and (iv) heterogeneous land surfaces respectively, the latter two of which include urban surfaces. However, techniques for retrieving aerosol over low-reflecting surfaces of water and vegetation are better developed than those over land, because assumptions can be made that the surface reflectance is either zero or near zero. Based on this, Kaufman and Tanré (1988) developed an algorithm which first uses the NDVI (Normalized Difference Vegetation Index) to detect dense dark vegetation (DDV) pixels, then used the short-wave infrared (SWIR, 2.1 μm) band, which is not affected by aerosol, to obtain the surface reflectance for the DDV pixels. Then based on the relationship

$$Lsurf_{0.49} = 0.25 * Lsurf_{2.1}$$
$$Lsurf_{0.66} = 0.5 * Lsurf_{2.1} \quad \text{(Kaufman and Sendra 1988),}$$

the apparent surface reflectance in the blue (0.49 μm) and red (0.66 μm) bands can be obtained. The difference between the actual surface reflectance in these bands and the observed (top of the atmosphere, TOA) reflectance is assumed to be due to aerosol. This amount is then fitted to a best-fit aerosol model, with knowledge of the expected aerosol types in the study area—for example, continental, industrial/urban, biomass burning, and marine—to arrive at AOD from the image blue and red wavebands.

From this DDV concept, NASA developed the MODIS Dark Target (DT) AOD product (MOD04; Kaufman and Tanré 1998) covering the globe. Although the DT product at 10 km spatial resolution only provides meaningful depictions on a broad regional scale, it is capable of giving an overview of air-quality conditions prevailing over a city's region. The expected error (EE) of the DT algorithm is $\pm (0.05 + 0.15 \times$ AOD) (Levy et al. 2013), which represents about 66% of retrievals within the EE on a global scale (Levy et al. 2010). The most recent version of the DT algorithm is the MODIS Collection 6.1 (C6.1) AOD product (Bilal et al. 2018a; Gupta et al. 2016). The C6.1 product addresses uncertainties due to the heterogeneity of urban surfaces, and updates the surface reflectance ratios using NASA's MOD09 surface reflectance product, which newly incorporates information on land cover type for pixels with

urban cover > 20% (Gupta et al. 2016). The Deep Blue (DB) AOD retrieval algorithm (Hsu et al. 2004) provides estimates of AOD over bright urban and desert, as well as dark surfaces, using the deep blue channels 412 and 470 µm in which these surfaces appear dark, as well as the red channel (0.65 µm) for dark surfaces. The EE of DB depends on geometry (Hsu et al. 2013; Sayer et al. 2013). The MODIS C6 product (including DT and DB algorithms) has been evaluated over urban areas with varying accuracies. For example, over Beijing, both the DT and DB C6 products (MOD04 and MYD04) were found to overestimate during highly polluted days due to a large error in the surface reflectance estimation (Bilal and Nichol 2015; Tao et al. 2015).

Within C6, a combined DT/DB algorithm has also been produced at 10 km, which combines both DT and DB algorithms in the same image, to retrieve AOD over both dark and bright surfaces including urban areas (Levy et al. 2013). However, accuracy over Asian cities was observed to be low, with only 57% of retrievals falling within the expected error. Bilal et al. (2017) introduced a customized algorithm which specifies the use of the DB algorithm when NDVI > 0.3, which cancels out the tendency of the DT and DB algorithms respectively, to under- and overestimate the surface reflectance, and which improved the percentage of retrievals within the expected error to 65%.

Although both DT and DB algorithms use MODIS 500 m resolution wavebands, their AOD products are produced at the spatial resolution of 10 km because the 500 m pixels are amalgamated into windows of 20 × 20 (400) pixels to increase the signal-to-noise ratio. Then, to eliminate clouds and water surfaces, dark and bright pixels, which are unsuitable for retrieval of AOD, are deselected, with at most 120 pixels remaining. Because the MODIS DT and DB products are unable to resolve city-level features, the MODIS aerosol team produced a global DT product at 3 km, the MOD04_3K/MYD04_3K, within the operational C6 aerosol product (Remer et al. 2013). Comparison with AERONET (AErosolRObaticNETwork) ground stations suggests that the MOD_3K is less reliable than the 10 km products (Bilal et al. 2018b). This may be because only a maximum of 11 pixels remain in the deselection window, making the product noisier than that at 10 km.

Yang et al. (2018) conducted a preliminary investigation of an AOD product at 1 km resolution using the geostationary Advanced Himawari Imager (AHI) satellite, based on the DT algorithm, with results showing some overestimation compared to AERONET data, with a correlation coefficient of 0.83 and RMSE of 0.11. Due to the recent availability of AHI, the AOD retrievals could not be thoroughly evaluated but are considered promising. In view of the superior temporal resolution of geostationary satellites (10-minutes for AHI), along with future improvement in spatial resolution, semi-continuous monitoring of particulate concentrations at the city district scale will be possible.

Contributions of the DB and DT retrievals to future global aerosol monitoring projects such as ESA's EarthCARE mission (Illingworth et al. 2015), with 10 km radar and LiDAR, WMO's GALION project, a ground-based aerosol LiDAR system (Bösenberg et al. 2008), ESA's ADM-AEOLUS mission, a space-based wind profiler system launched in 2018 (Lolli et al. 2013), and NASA's on-going CALIPSO mission with satellite-based aerosol LiDAR (Winker et al. 2010), will be very important.

As with AOD retrieval, the estimation of other gaseous pollutants from satellite-image wavebands is constrained by the weakness of the signal relative to the total image reflectance, thus necessitating large pixel sizes. The MOPITT (Measurement of Pollution in the Troposphere) sensor, which measures CO emissions from the Earth's surface, has 22 km spatial resolution at nadir, and OMI (Ozone Monitoring Instrument) for ozone and NO_2 estimation with a spatial resolution of 13 km $\times$ 24 km, are not readily applicable for retrieval of urban-scale pollutant concentrations. Although Bechle (2013) found that the OMI sensor aboard NASA's Aura satellite was able to measure spatial variability in NO_2 exposure over a large urban area, detailed district-level concentrations were constrained by the coarse resolution of the sensor. These constraints have been lessened somewhat by the TROPOMI sensor onboard the European Space Agency's Sentinel 5P satellite launched in October 2017, which measures ozone, NO_2, SO_2, methane, and CO at 7 km $\times$ 3.5 km resolution. However, this is still too coarse for application at urban scales, and since algorithms developed for complex land areas are difficult to apply, the task of deriving accurate air-quality products for urban areas remains challenging.

16.2 Remote Sensing of the Urban Heat Island

Urban heat islands are caused by the replacement of natural evaporative and porous land surfaces with non-evaporative human-made surfaces (Chandler 1965). These disperse a much greater proportion of energy received into the surrounding atmosphere as sensible heat, compared with the predominantly latent heat loss of rural surfaces. Along with the generally lower albedo of urban surfaces, this results in significantly higher air temperatures in cities compared with their rural surroundings, and the difference ($\Delta T(u\text{-}r)$) reaches a maximum at night. As most cities have few air-monitoring stations, the level of detail of intra-city temperatures is inadequate, whereas satellite thermal data provide a dense grid of continuous and time-synchronized land surface temperatures (LSTs) over a whole city. Since cities are identifiable on thermal satellite images for their temperature contrasts, as much as for their optical differences with surrounding rural areas, many remote-sensing studies have taken place (Roth et al. 1989; Weng 2009; Zhou et al. 2019). However, there are numerous constraints to the use of the data in urban climatology, which are discussed below.

16.2.1   Spatial Resolution of Satellite Sensors Related to Scales of Urban Climate

Due to the inverse relationship between wavelength and signal strength, longer-wavelength thermal infrared sensors generally have a coarse resolution. Therefore the thermal waveband of MODIS, at 1 km resolution, has only been used for general temperature-trend analysis over city regions (Bonafoni 2016; Hulley et al. 2014). The 60 m and 90 m resolution sensors of Landsats 5–7/8 and 90 m of ASTER have also been used for urban climatic analysis at the district and even the street scale within cities (Nichol 1996a; Nichol et al. 2009; Feng and Myint 2016; Meng et al. 2018). To overcome the limitation of spatial resolution, various ways of disaggregating the thermal signal to provide more spatial detail have been presented (Nichol 2009; Rodriguez-Galliano et al. 2012; Zhou et al. 2019). Figure 16.1 shows the effects of emissivity modulation on an ASTER thermal image of a suburban area of Hong Kong. The original resolution of 90 m (Fig. 16.1c) is disaggregated to a 10 m pixel size (Fig. 16.1a), while correcting for surface emissivity differences (Nichol et al. 2009).

16.2.2   Relationship Between Surface Temperature and Air Temperature

The conception as well as the usefulness of the UHI concept derives from its representation of urban air temperatures which affect human comfort. More specifically these are air temperatures within the urban canopy layer comprising the space within streets between the surface and the top of the buildings (Oke 1976). However, satellite thermal sensors measure the surface radiometric temperature or land surface temperature (LST). Thus, the surface heat island (SUHI) represents the radiometric temperature difference between urban and non-urban surfaces (Zhou et al. 2019). Since the satellite-derived heat island is based on LST, the optimum usefulness of these data depends on defining their relationship to a more conventional view of the urban heat island, such as screen-level air temperature at the time of imaging (Nichol et al. 2009; Schwarz et al. 2012; Clay et al. 2016). Li et al. (2018) developed an air-temperature dataset at 1 km resolution covering the entire USA by combining daily air-temperature data from weather stations with gap-filled MODIS LST data and an elevation model. The method proved satisfactory, generating root mean square errors of 2.1 and 1.9 °C, and R^2 of 0.95 and 0.97 for daily minimum and maximum air temperature, respectively. Sun et al. (2015) estimated air temperatures over Beijing from MODIS LST data combined with vegetation indices, obtaining accuracies of approximately 2°K compared with weather station data.
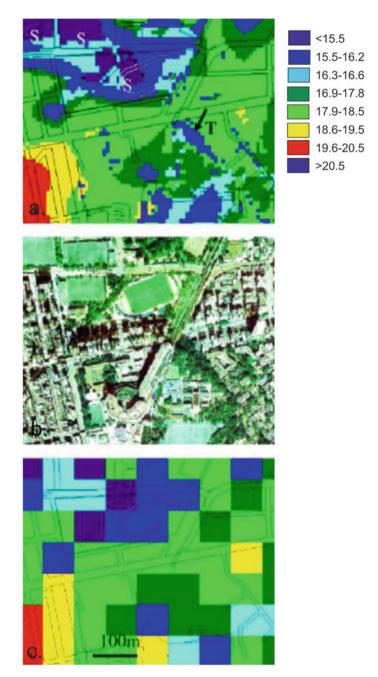
Fig. 16.1 Surface temperatures of a mixed urban/suburban district in Hong Kong from: **a** ASTER nighttime thermal image at 10.42 pm on 31.01.07 after emissivity modulation, **b** Aerial photograph showing land cover types, **c** Original ASTER thermal image with 90 m resolution

16.2.3   Time of Imaging in Relation to Heat Island Maximum

Most space-borne thermal sensors such as the Landsat series and ASTER record mainly during the daytime when densely built, high-rise areas may constitute a heat sink (Nichol 2005; Rasul et al. 2017). Tropical cities (Nichol 2003) or arid zones in summertime (Nassar et al. 2016; Rasul et al. 2017) may also exhibit heat sinks during the day. Furthermore, the timing of the satellite overpass may not be ideal for detecting temperature differences. Landsat for example at 9.30–10.30 am local time is near the morning thermal crossover time when minimal thermal contrasts would be expected. Differences in surface temperature are largest during the daytime, thus the surface heat island based on LST is more pronounced than that of the conventional UHI based on air temperature, for which the greatest differences are at night (Nichol 2005). Additionally, Sun et al. (2015) observed that LST was more similar to air temperatures within the urban canopy layer at night but considerably different during the day. The relationship may even be negative, as LST in urban districts increases due to early-morning warming, while high-rise urban districts in shadow when the sun angle is still low may constitute a heat sink (Nichol 2005).

   In changing environmental conditions, satellite images taken at a single instant may be unrepresentative. However, Nichol and To (2012) found that in Hong Kong, due to a more stable boundary layer at night, nighttime ASTER thermal images were representative of commonly occurring climatic conditions for a 13-h period surrounding the image acquisition time, and were significantly correlated with ground air temperatures over the city, for 93% of hot summer nights.

16.2.4   Anisotropy of the Satellite View

Satellites record the temperature of horizontal surfaces, which may only represent the complete radiating surface in flat rural areas. The effective (active) surface area of a city, especially in high-rise areas, and using narrow field-of-view sensors, is much larger than the equivalent countryside of the same size (Voogt and Oke 1996). In high-rise housing estates in Singapore, for example, the active surface was found to be 1.7 times greater than the planimetric (satellite seen) surface (Nichol 1998). Thus nadir views would be warmer or cooler than off-nadir views depending on the sun position. Hu et al. (2016) quantified anisotropic effects for two high-rise cities— New York and Chicago—observing that daytime maximum temperature bias due to anisotropy was up to 9°K for the most urbanized areas. When averaged over the entire SUHI as measured by MODIS LST, the UHI magnitude was modified by 2.3°K, that is, 25–30%, due to surface anisotropy. Voogt and Oke (1996) recommended using ground-based observations to construction models for the weighting of temperatures according to area and sun position (see also Nichol et al. 2014).

16.2.5 *The Need for Emissivity and Atmospheric Correction*

Although satellite-derived radiance values can readily be converted to equivalent black-body temperature (or brightness temperature) using Planck's Law, this underestimates the surface radiometric temperature if corrections for emissivity differences according to the type of land cover are not carried out. For example, a metal roof of emissivity 0.92, and tile roof of emissivity 0.98, both with a radiometric temperature of 27 °C, will have brightness temperature (image) values of 20.8 and 25.5 °C respectively. However for UHI studies, measurement of individual surface temperatures is both impossible and unnecessary, as emitted radiation from each pixel is an aggregated value of all surfaces within the pixel, and subject to anisotropic effects according to look angle and the pixel's horizontal/vertical surface ratio. To address this, Yang et al. (2015, 2016) developed an urban emissivity model based on the sky view factor (SVF), which accounted for surface material type and building geometry, and found that a decrease in SVF was accompanied by increased emissivity due to multiple scattering among buildings. Another potential source of error in thermal image values is that they can only be considered accurate in clear, dry atmospheres, and a further correction using atmospheric data in a radiative transfer model such as MODRAN (Berk et al. 2014) should be made, if absolute temperatures are desirable. In humid atmospheres, energy absorption by atmospheric water vapor may account for brightness temperatures up to 15 °C cooler than the surface radiometric temperature (Nichol 1996b).

16.3 Monitoring Water Quality Along Urban Coastlines

Coastal waters are spatially complex, as they comprise a mixture of both saline and brackish water, as well as containing different types of land runoff. Urban coastlines are especially complex due to additional anthropogenic inputs, from both point and non-point sources, with often severe impacts on water quality (WQ). For this reason, WQ along urban coasts is subject to greater spatial and temporal variability than other coastlines, and WQ monitoring from remote-sensing platforms requires sensors with fine spatial as well as temporal resolution. A further challenge is due to the wide range of organic and inorganic inputs to urban coastal waters making them optically complex for ocean color monitoring. A common problem in countries with unregulated drainage is high nutrient inputs from agricultural, industrial, and urban waste, resulting in eutrophication and algal bloom events. These may be toxic to humans as well as affecting a wide variety of marine organisms.

Due to these factors, sensors frequently used for marine applications such as the Sea-Viewing Wide-Field-of-View Sensor (SeaWiFS), the Moderate Resolution Imaging Spectroradiometer (MODIS), the Visible and Infrared Imager/Radiometer Suite (VIIRS), the Geostationary Ocean Color Imager (GOCI), and the Ocean and Land Color Imager (OLCI), with spatial resolutions of several hundred meters, are unable to resolve the necessary spatial detail, although they may have good temporal and spectral resolutions. Recent space-based sensors with moderate resolution used for retrieval of water-quality indicators (WQIs) include NASA's Landsat, the Chinese HJ1 A/B, and ESA's Sentinel series. The most recent Landsat 8 carries the Operational Land Imager (OLI), with 9 spectral wavebands, 5 in the optical spectrum from 430–880 nm, which are being used for ocean color monitoring (Franz et al. 2015; Vanhellemont and Ruddick 2015). OLI has 30 m spatial resolution and a repeat cycle of 16 days, which is increased to 8 days if combined with Landsat 7. The MultiSpectral Instrument (MSI) on ESA's Sentinel-2 platform carries 12 wavebands, including three ocean color bands, blue (490 nm), green (560 nm) and red (665 nm) at 10 m resolution, and three Near InfraRed (NIR) bands (705–783 nm) at 20 m resolution. OLI has a 16-day repeat cycle.

Clear water shows low reflectance in the visible spectrum and absorbs most energy in the NIR region, but the optical properties of water are affected by a range of substances. These have given rise to the concept of ocean color sensing (Morel and Prieur 1977), as dissolved organic matter (DOM) is strongly absorptive in the blue (490 nm) spectral region, chlorophyll-a (Chl-a) in phytoplankton and algal pigments mainly absorbs sunlight in the blue and red regions of the spectrum, and suspended solids (SS) mainly reflect in the red and NIR regions (600–800 nm). Due to the difficulty of retrieving an adequate reflected signal from the water column which absorbs most light energy, the atmospheric component may be dominant unless it is first removed, thus atmospheric correction is an essential pre-processing step (Pahlevan et al. 2017). Algorithms for retrieval of WQIs from the water column have undergone refinement as the spatial and spectral resolutions of space-borne sensors and computing power have improved. Improvements in temporal resolution with more satellite sensors and more frequent repeat cycles have released more data for testing and validation of retrievals, which require close synchronization with sea-station data (Pahlevan et al. 2019). Algorithms for retrieval of WQPs are usually based on obtaining a substantial number of synchronous image and station samples for regression against image wavebands, and a further substantial number for validating the results.

For example, a study of water quality around the heavily urbanized coastlines of Hong Kong and the Pearl River Delta (PRD; Nazeer and Nichol 2016a) was able to obtain 240 co-located samples of Chl-a and SS within two hours of image acquisition when combining images from Landsat TM/ETM + and HJ1 A/B sensors over a 13-year period (2000 to 2012). However due to the complexity of the coastal waters, with PRD river sediments to the west, urban runoff in the central section, and clear waters of the South China Sea to the east, retrieval algorithms developed across the whole region were less accurate than those applied to individual water-quality zones delineated by fuzzy *c*-means clustering. Thus, for Chl-a a low root mean square error (RMSE) of 1.61 µg/l was obtained for individual water-quality zones compared with 4.59 µg/l when applied to the whole spectrum of different water types across the region. For SS concentrations, a significant improvement was also observed, with the RMSE reducing from 2.72 mg/l to 1.19 mg/l when the models were applied to individual zones. These results are good, considering the wide range of concentrations obtained in the ship-sampled datasets, namely a Chl-a range of 0.30 to 13.0 µg/l and SS concentration range of 0.5 to 56.0 mg/l, and suggest that space-borne sensors are capable of providing spatially detailed, accurate, and cost-effective water-quality status around urban coastlines.

With urbanization of coastlines, an increasing incidence of red tide events caused by massive algal blooms from high nutrient inputs is being seen around the world, but especially in rapidly urbanizing parts of Asia such as China and the Philippines (Azanza et al. 2008; Nazeer et al. 2017). Such events are toxic to the marine ecosystem and pose dangers to human health; thus, environmental authorities need timely and detailed information on their occurrence. However, since the occurrence of a red tide does not usually correspond with routine ship-borne water sampling missions (monthly in Hong Kong), many go undetected. In Hong Kong, which is a thriving international port but still has diverse coastal ecosystems, a severe red tide event from December 2015 to February 2016 saw 220 tons of fish kills reported (SCMP 2016). A remote sensing study of chlorophyll-a concentrations around the complex coastal waters of Hong Kong using Landsat TM/ETM + (Fig. 16.2; Nazeer and Nichol 2016b) observed that a ratio of the red (630–690 nm) with the square of the blue (450–520 nm) bands were most capable of representing actual Chl-a concentrations due to the differential response of the red and blue wavebands to the Chl-a signal. A correlation coefficient of 0.89 and mean absolute error (MAE) of 1.02 µg/l obtained for the study indicated a good degree of confidence in remote sensing for routine monitoring of red tide events along urban coastlines.
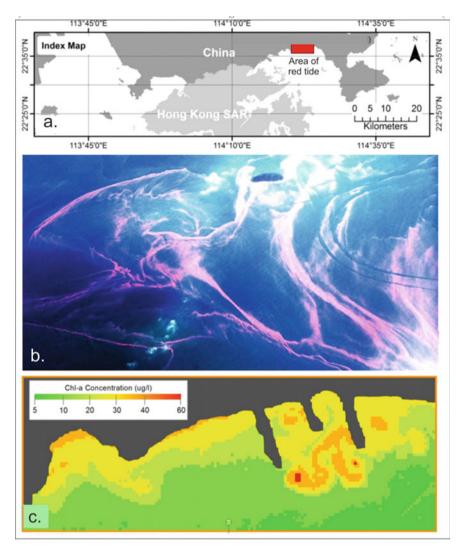
Fig. 16.2 Red tide along the Chinese coast adjacent to Hong Kong, on 25th November 2014.
a Location of red tide, **b** Aerial photograph of red tide (photo credits Xinhua), **c** Chl-a concentration
map in µg/l of red-tide-affected area using the ratio of Landsat/HJ1 blue (450–520 nm) and red
bands(630–690 nm)

References

Azanza RV, David LT, Borja RT, Baula IU, Fukuyo Y (2008) An extensive Cochlodinium bloom along the western coast of Palawan, Philippines. Harmful Algae 7:324–330. https://doi.org/10.1016/J.HAL.2007.12.011

Bechle (2013) Remote sensing of exposure to NO_2: satellite versus ground-based measurement in a large urban area. Atmos Environ 69:345–353

Berk A, Conforti P, Kennett R, Perkins T, Hawes F, van den Bosch J (2014) MODTRAN6: a major upgrade of the MODTRAN radiative transfer code. In: Proceedings of SPIE 9088, Algorithms and Technologies for Multispectral, Hyperspectral, and Ultraspectral Imagery. p. 20: 90880H. https://doi.org/10.1117/12.2050433

Bilal M, Nichol JE (2015) Evaluation of MODIS aerosol retrieval algorithms over the Beijing-Tianjin-Hebei region during low to very high pollution events. J Geophy. Res. Atmos 120:7941–7957. https://doi.org/10.1002/2015JD023082

Bilal M, Nichol JE, Wang L (2017) New customized methods for improvement of the MODIS C6 dark target and deep blue merged aerosol product. Remote Sens 197:115–124. https://doi.org/10.1016/j.rse.2017.05.028

Bilal M, Nazeer M, Qiu Z, Ding X, Wei J (2018a) Global validation of MODIS C6 and C6.1 merged aerosol products over diverse vegetated surfaces. Remote Sens 10(3):475. https://doi.org/10.3390/rs10030475

Bilal M, Qiu Z, Campbell JR, Spak S, Shen X, Nazeer M (2018b) A new MODIS C6 dark target and deep blue merged aerosol product on a 3 km spatial grid. Remote Sens 10:463. https://doi.org/10.3390/rs10030463

Bonafoni S (2016) Downscaling of Landsat and MODIS land surface temperature over the heterogeneous urban area of Milan. IEEE J Sel Top. Appl Earth Obs Remote Sens 9:2019–2027

Bösenberg J, Hoff R, Ansmann A, Müller D, Antuña JC, Whiteman D, Sugimoto N, Apituley A, Hardesty M, Welton Jet al. (2008) GAW aerosol lidarobservation network (GALION). WMO, Geneva, Switzerland

Chandler TJ (1965) The climate of London. Hutchinson, London

Clay R, Guan H, Wild N, Bennett J, VinodkumarEwenz C (2016) Urban heat island traverses in the city of Adelaide, South Australia. Urban Clim. 17:89–101

Feng X, Myint SW (2016) Exploring the effect of neighboring land cover pattern on land surface temperature of central building objects. Build Environ 95:346–354

Franz BA, Bailey SW, Kuring N, Werdell PJ (2015) Ocean color measurements with the Operational Land Imager on Landsat-8: implementation and evaluation in SeaDAS. J Appl Remote Sens 9(1):096070. https://doi.org/10.1117/1.JRS.9.096070

Gupta P, Levy RC, Mattoo S, Remer LA, Munchak LA (2016) A surface reflectance scheme for retrieving aerosol optical depth over urban surfaces in MODIS Dark Target retrieval algorithm. Atmos Meas Tech 9:3293–3308. https://doi.org/10.5194/amt-9-3293-2016

Hsu NC, Tsay SC, King MD, Herman JR (2004) Aerosol properties over bright-reflecting source regions. IEEE Trans Geosci Remote Sens 42:557–569

Hsu NC Jeong MJ, Bettenhausen C, Sayer AM, Hansell R, Seftor CS, Huang J, Tsay SC (2013) Enhanced deep blue aerosol retrieval algorithm: the second generation. J Geophys Res Atmos 118:9296–3015

Hu L, Monaghan A, Voogt JA, Barlage M (2016) A first satellite-based observational assessment of urban thermal anisotropy. Remote Sens Environ 181:111–121

Hulley G, Veraverbeke S, Hook S (2014) Thermal-based techniques for land cover change detection using a new dynamic MODIS multispectral emissivity product (MOD21). Remote Sens Environ 140:755–765

Illingworth AJ, Barker HW, Beljaars A, Ceccaldi M, Chepfer H, Clerbaux N, Cole J, Delanoë J, Domenech C, Donovan DP et al (2015) The Earthcare satellite: The next step forward in global measurements of clouds, aerosols, precipitation, and radiation. Bull Am Meteor Soc 96:1311–1332

Kaufman YJ, Tanré D (1998) Algorithm for remote sensing of tropospheric aerosols from MODIS. NASA MODIS algorithm theoretical basis document. Goddard Space Flight Cent 85(1998):3–68

Levy RC, La Remer, Kleidman RG, Mattoo S, Ichoku C, Kahn R, Eck TF (2010) Global evaluation of the Collection 5 MODIS dark-target aerosol products over land. Atmos Chem Phys 10:10399–10420

Levy RC, Mattoo S, Munchak LA, Remer LA, Sayer AM, Patadia F, Hsu NC (2013) The Collection 6 MODIS aerosol products over land and ocean. Atmos Meas Tech 6:2989–3034

Li X, Zhou Y, Asrar GR, Zhu Z (2018) Developing a 1 km resolution daily air temperature dataset for urban and surrounding areas in the conterminous United States. Remote Sens Environ 215:74–84

Lolli S, Delaval A, Loth C, Garnier A, HFP (2013) 0.355-micrometer direct detection wind lidar under testing during a field campaign in consideration of ESA's ADM-Aeolus mission. Atmos Meas Tech 6:3349–3358

Meng Q, Zhang L, Sun Z, Meng F, Wang L, Sun Y (2018) Characterizing spatial and temporal trends of surface urban heat island effect in an urban main built-up area: A 12-year case study in Beijing, China. Remote Sens Environ 204:826–837

Morel A, Prieur L (1977) Analysis of variations in ocean color. Limnol Oceanogr 22:709–722. https://doi.org/10.4319/lo.1977.22.4.0709

Nassar AK, Blackburn GA, Whyatt JD (2016) Dynamics and controls of urban heat sink and island phenomena in a desert city: development of a local climate zone scheme using remotely-sensed inputs. Int J Appl Earth Obs Geoinf 51:76–90

Nazeer M, Nichol JE (2016a) Improved water quality retrieval by identifying optically unique water classes. J Hydrol 541:1119–1132. https://doi.org/10.1016/j.jhydrol.2016.08.020

Nazeer M, Nichol JE (2016b) Development and application of a remote sensing-based Chlorophyll-a concentration prediction model for complex coastal waters of Hong Kong. J Hydrol 532:80–89. https://doi.org/10.1016/j.jhydrol.2015.11.037

Nazeer M, Wong MS, Nichol JE (2017) A new approach for the estimation of phytoplankton cell counts associated with algal blooms. Sci Total Environ 590:125–138. https://doi.org/10.1016/j.scitotenv.2017.02.182

Nichol JE (1996a) High resolution surface temperature patterns related to urban morphology of in a tropical city: a satellite-based study. J Appl Meteorol 35(1):135–146

Nichol JE (1996b) Analysis of the urban thermal environment of Singapore using LANDSAT data. Environ Plan 23:733–747

Nichol JE (1998) Visualisation of urban surface temperatures derived from satellite images. Int J Remote Sens U.K. 19(9):1639–1649

Nichol JE (2003) Heat island studies in the third world cities using GIS and remote sensing. Chapter 13. In: MesevV (ed) Remotely sensed cities. Taylor and Francis

Nichol JE (2005) Remote sensing of urban heat islands by day and night. Photogram Eng Remote Sens 71(5):613–621

Nichol JE (2009) An emissivity modulation method for spatial enhancement of thermal satellite images in urban heat island analysis. Photogram Eng Remote Sens 75(5):547–556

Nichol JE, Fung WY, Lam KS, Wong MS (2009) Urban heat Island diagnosis using ASTER satellite images and 'in situ' air temperature. Atmos Res 94:276–284

Nichol JE, To PH (2012) Temporal characteristics of thermal satellite images for urban heat stress and heat island mapping. ISPRS J Photogram Remote Sens 74:152–162

Nichol J, Bilal M, Ashley WWS (2014) Retrieval of Aerosol Optical Thickness (AOT) from urban shadows using fine resolution WorldView-II images. In: Remote sensing and photogrammetry society annual conference, Aberystwyth, 02–05 Sept

Oke TR (1976) The distinction between canopy and boundary-layer heat islands. Atmosphere 14:268–277

Pahlevan N, Chittimalli SK, Balasubramanian SV, Vellucci V (2019) Sentinel-2/Landsat-8 product consistency and implications for monitoring aquatic systems. Remote Sens Environ 220:19–29. https://doi.org/10.1016/J.RSE.2018.10.027

Pahlevan N, Schott JR, Franz BA, Zibordi G, Markham B, Bailey S, Schaaf CB, Ondrusek M, Greb S, Strait CM (2017) Landsat 8 remote sensing reflectance (Rrs) products: Evaluations, intercomparisons, and enhancements. Remote Sens Environ 190:289–301. https://doi.org/10.1016/J.RSE.2016.12.030

Rasul A, Balzter H, Smith C, Remedios J, Adamu B, Sobrino JA, Srivanit M, Weng Q (2017) A review on remote sensing of urban heat and cool islands. Land 6:38. https://doi.org/10.3390/land6020038

Remer LA, Mattoo S, Levy RC, Munchak LA (2013) MODIS 3 km aerosol product: algorithm and global perspective. Atmos Meas Tech 6:1829–1844

Rodriguez-Galiano VF, Pardo-Igúzquiza E, Chica-Olmo M, Mateos J, Juan P, Rigol-Sánchez JP, Vega M (2012) A comparative assessment of different methods for Landsat 7/ETM + pansharpening. Int J Remote Sens 33(20):6574–6599. https://doi.org/10.1080/01431161.2012.691612

Roth M, Oke TR, Emery WJ (1989) Satellite derived urban heat islands from three coastal cities and the utilisation of such data in urban climatology. Int J Remote Sens 10(11):1699–1720

Sayer AM, Hsu NC, Bettenhausen C, Jeong MJ (2013) Validation and uncertainty estimates for MODIS collection 6 "deep blue" aerosol data. J Geophys Res Atmos 118:7864–7872

Schwarz N, Schlink U, Franck U, Grossmann K (2012) Relationship of land surface and air temperatures and its implications for quantifying urban heat island indicators—An application for the city of Leipzig (Germany). Ecol Ind 18:693–704

South China Morning Post (SCMP) 2016 Hong Kong fish farmers claim proliferation of red tides is worst 'UnnaturalDisaster' to hit industry in years, 30th April 2016

Sun H, Chen Y, Zhan W (2015) Comparing surface- and canopy-layer urban heat islands over Beijing using MODIS data. Int J Remote Sens 36:5448–5465

Tao M, Chen L, Wang Z, Tao J, Che H, Wang X, Wang Y (2015) Comparison and evaluation of the MODIS collection 6 aerosol data in China. J Geophys Res Atmos 120:6992–7005

Vanhellemont Q, Ruddick K (2015) Advantages of high quality SWIR bands for ocean colour processing: examples from Landsat-8. Remote Sens Environ 161:89–106. https://doi.org/10.1016/j.rse.2015.02.007

Voogt JA, Oke TR (1996) Complete urban surfacetemperatures. In: Proceedings of the 12th conference on biometeorology and aerobiology. American Meteorological Society, Atlanta, USA, pp 438–441

Weng Q (2009) Thermal infrared remote sensing for urban climate and environmental studies: Methods, applications, and trends. ISPRS J Photogram Remote Sens 64:335–344

Winker DM, Pelon JAC Jr, Ackerman SA, Charlson RJ, Colarco PR, Flamant P, Fu Q, Hoff RM, Kittaka C et al (2010) The calipso mission. Bull Am Meteor Soc 91:1211–1230

Yang F, Wang Y, Tao J, Wang Z, Fan M, de Leeuw G, Chen L (2018) Preliminary investigation of a new AHI Aerosol Optical Depth (AOD) retrieval algorithm and evaluation with multiple source AOD measurements in China. Remote Sens 10:848. https://doi.org/10.3390/rs10050748

Yang J, Wong MS, Menenti M, Nichol J (2015) Modeling the effective emissivity of the urban canopy using sky view factor. ISPRS J Photogram Remote Sens 105:211–219

Yang JX, Wong MS, Menenti M, Nichol JE, Voogt J, Krayenhoff ES (2016) Development of an improved urban emissivity model based on sky view factor for retrieving effective emissivity and surface temperature over urban areas. ISPRS J Photogram Remote Sens 122:30–40

Zhou D, Xiao J, Bonafoni S, Berger C, Deilami K, Zhou Y, Frolking S, Yao Y, Qiao Z, Sobrino JA (2019) Satellite remote sensing of surface urban heat islands: progress, challenges, and perspectives. Remote Sens 11:48. https://doi.org/10.3390/rs11010048

Janet E. Nichol is an Applied Geographer, specializing in Remote Sensing, Geo-Informatics, and Environmental Change. Her main research interests are in the application of remote sensing to urban areas and landscape change, especially in the context of global climatic change. She has previously worked in universities in Nigeria, the Republic of Ireland, Singapore, and Hong Kong, and is currently a Visiting Professor at the University of Sussex, UK.

Muhammad Bilal is a Professor of Remote Sensing at the Nanjing University of Information Science and Technology (NUIST), Nanjing, China. In October 2018, the Jiangsu Provincial Education Department conferred on him the special title of "Distinguished Professor" based on his outstanding research achievements.

Majid Nazeer is serving as Associate Professor at the Key Laboratory of Digital Land and Resources, East China University of Technology (ECUT), Nanchang, Jiangxi, China. His research interests include oceanic remote sensing, land cover and land use classification, spatial modeling, air pollution, and atmospheric correction of satellite imagery.

Man Sing Wong is an Associate Professor of the Department of Land Surveying and Geo-Informatics, The Hong Kong Polytechnic University, and also a NASA's AERONET Hong Kong station site manager. He is a chartered member of the Royal Institution of Chartered Surveyors, the Hong Kong Institute of Surveyors, and a Fulbright scholar supported by the United States Department of State. He has published over 100 SCI journals and received over HKD 58 million of research funding as PI in the last couple of years.